*Bangladesh Journal of Physics, Vol. **33**, Issue 1, pp. 25 – 49, June 2026*

IRREVERSIBILITY ANALYSIS AND MAGNETOHYDRODYNAMIC BIOCONVECTION OF MOTILE MICROORGANISMS IN EYRING-POWELL NANOFLUIDS WITH JOULE HEATING AND ARRHENIUS KINETICS

DIPTA ROY[1], MARIA RAHMAN[1], KAJAL CHANDRA SAHA[1*]

[1]*Department of Applied Mathematics, University of Dhaka, Dhaka 1000, Bangladesh*

Corresponding author: kcsaha@du.ac.bd

Received on 11.06.2026, Revised received on 27.06.2026, Accepted for publication on 30.6.2026

DOI: ***https://doi.org/10.3329/bjphy.v33i1.90771***

ABSTRACT

The present study brings forward a detailed numerical study that examines entropy-optimized bioconvective transport in chemically reacting Eyring-Powell nanofluids moving over stretching surfaces, which is considered in a Darcy-Forchheimer porous medium. The effects of thermophoresis and Brownian motion is included in the model together with the behavior of moving gyrotactic microorganisms through its implementation of nonlinear mixed convection, Arrhenius activation energy, and magnetohydrodynamic effects within the Buongiorno framework. A high-order collocation procedure is used for the numerical solution of the governing equations. The results demonstrate that thermal and concentration Grashof numbers create an increase in fluid velocity because they produce stronger buoyancy effects. The combination of the magnetic parameter with the Eyring rheological parameters leads to reduced flow momentum because of resistance from Lorentz forces. Internal heat generation and Joule heating enhance thermal transport, while increased thermophoresis and Brownian motion reduce the local Nusselt number. Microorganism density shows high sensitivity to Péclet and bioconvection Lewis numbers, with higher values thinning the bioconvection layer. Entropy analysis reveals that irreversibility reaches its highest level near the surface, primarily due to the combined effects of fluid friction, porous medium resistance, and magnetic field–induced energy dissipation. These insights contribute to a better understanding of the underlying transport mechanisms and may support the design and optimization of bio-thermal systems, including microbial fuel cells and advanced cooling technologies.

Keywords: *Eyring–Powell nanofluid, Bioconvective transport, Entropy generation analysis, Arrhenius activation energy*

1. Introduction

The rapid growth of modern technologies has placed increasing demands on thermal management systems, creating a strong need for heat-transfer fluids with superior cooling capabilities. Traditional heat-transfer fluids, including water, ethylene glycol, and mineral oils, are widely used in industrial applications; however, their relatively low thermal conductivity limits their effectiveness in high-performance thermal systems [1, 2]. To address this limitation, Choi and Eastman introduced the concept of nanofluids, which are formed by dispersing nanosized solid particles into a base fluid [3]. This innovation opened a new avenue for enhancing thermal transport properties and significantly improving heat transfer performance. As a result, nanofluids have gained significant interest due to their enhanced thermal characteristics for applications ranging from electronic cooling and solar thermal collectors to advanced energy conversion and power-generation systems [4, 5].

A proper understanding of nanofluid transport requires careful consideration of the mechanisms governing nanoparticle motion within the carrier fluid. In this regard, Buongiorno [6] developed a pioneering non-homogeneous model that identified Brownian diffusion and thermophoresis as the two dominant slip mechanisms that drive the motion of nanoparticles relative to the base fluid [7, 8]. Brownian motion originates from random molecular collisions, while thermophoresis drives particles from hotter regions toward cooler ones under the influence of temperature gradients. These transport mechanisms play a vital role in enhancing energy exchange and have therefore become important in thermal systems such as laser devices, microwave components, and other high-heat-flux technologies [9–12]. Furthermore, the incorporation of magnetic nanoparticles into nanofluids has enabled significant advances in biomedical engineering, including targeted drug delivery, cancer hyperthermia treatments, and thermal control in robotic surgical systems [13–15].

Although Newtonian fluid models adequately describe many engineering flows, numerous industrial fluids exhibit rheological behaviors that cannot be captured by a simple linear correlation between stress and strain rate. Materials exhibiting this behavior are commonly observed in polymer melts, lubricants, paints, biofluids, and numerous chemical mixtures [16, 17]. Such fluids belong to the class of non-Newtonian materials and require more sophisticated constitutive models for accurate prediction of their flow behavior [18]. Among the available models, the Eyring–Powell formulation has gained particular interest because it is derived from kinetic theory and successfully captures fluid behavior across a wide range of shear rates [19–21]. Unlike empirical power-law models, the Eyring–Powell model is capable of representing Newtonian characteristics at both low and high shear rates while preserving shear-thinning effects in the intermediate regime [22, 23]. Recent investigations have demonstrated that the rheological properties described by this model substantially influence boundary-layer development and thermal transport, especially in flows over stretching surfaces [24].

Another emerging area of interest is the coupling of nanofluids with bioconvection phenomena. Bioconvection arises from the collective behavior of motile microorganisms, particularly gyrotactic algae and bacteria, suspended within a fluid medium [25, 26]. These microorganisms often possess a slightly higher density than the surrounding fluid and tend to migrate upward in response to environmental cues such as gravity and oxygen concentration gradients. As microorganisms accumulate near the upper region of the suspension, density stratification develops and eventually becomes unstable, leading to organized convective patterns known as bioconvection cells [27–30]. From an engineering perspective, the presence of motile microorganisms offers an additional benefit by reducing nanoparticle sedimentation and improving the long-term stability of nanofluids [31]. Consequently, bioconvective nanofluid systems have attracted considerable interest in applications such as biofuel production, bioreactors, and enhanced oil recovery technologies [32–34].

The application of magnetic fields provides another effective strategy for controlling fluid transport processes. In magnetohydrodynamic (MHD) systems, the interaction between electrically conducting fluids and an external magnetic field generates a Lorentz force that modifies the flow structure and boundary-layer characteristics [35–38]. When combined with bioconvection, magnetic effects offer an additional mechanism for regulating fluid motion because the transport behavior is simultaneously influenced by buoyancy forces associated with nanoparticles and microorganisms [39]. Such controllable transport characteristics are particularly valuable in microfluidic devices, biomedical technologies, optical switching systems, and industrial filtration processes where precise flow regulation is required [40–42].

Many practical transport processes are also influenced by chemical reactions whose rates depend strongly on temperature and species concentration. The Arrhenius activation energy concept provides a fundamental framework for describing the minimum energy required to initiate a chemical reaction and is widely used in modeling processes related to geothermal systems, petroleum storage, and nuclear technologies [43]. Within boundary-layer flows, activation energy and chemical reaction effects can significantly alter nanoparticle concentration distributions and microorganism density profiles [44, 45]. Additional complexities arise from nonlinear thermal radiation and Stefan blowing effects, both of which can substantially modify heat and mass transfer characteristics near the surface [46, 47]. In particular, Stefan blowing becomes important in situations involving intense evaporation or species injection, where mass transfer at the wall alters the structure of the boundary layer.

Beyond transport enhancement, improving the thermodynamic efficiency of such systems has become a major research objective. According to the second law of thermodynamics, every real process is accompanied by irreversible losses arising from mechanisms such as fluid friction, heat transfer across finite temperature differences, and viscous dissipation. These losses can be quantified through entropy generation analysis, which provides an important framework for assessing system efficiency and detecting sources of thermodynamic irreversibility [48, 49]. Salawu et al. [50] emphasized the importance of entropy generation studies in understanding the influence of thermal gradients, Joule heating, and other dissipative effects on overall system efficiency [51, 52]. Through appropriate optimization of governing parameters such as magnetic field strength, stretching rate, and microorganism concentration, entropy production can be minimized, thereby enhancing the overall thermal performance of the system.

The analysis becomes even more challenging when mixed convection effects are included. In many practical situations, buoyancy forces arise not only from temperature differences but also from variations in nanoparticle concentration and microorganism density. This coupled buoyancy mechanism can either enhance or suppress the flow depending on the prevailing conditions and has a significant impact on wall shear stress, heat transfer characteristics, and mass transport rates [53]. Understanding these interactions is therefore essential for the development of efficient thermal systems, bio-thermal sensors, and chemically reactive transport devices employing non-Newtonian fluids.

Despite extensive studies on MHD nanofluids, bioconvection, non-Newtonian rheology, and entropy generation, the coupled effects of gyrotactic microorganisms, Darcy–Forchheimer porous media, Arrhenius activation energy, velocity slip, and nonlinear mixed convection on Eyring–Powell nanofluid transport remain largely unexplored. Moreover, the individual effects of thermal, frictional, and mass diffusion irreversibilities on the total thermodynamic performance of such systems remain insufficiently explored in a comprehensive manner. To address these limitations, the present work develops a unified model that integrates these physical mechanisms and provides a detailed entropy-based analysis through HTI, FFI, MDI, total entropy generation, and Bejan number. The findings offer new insight into irreversibility control and thermodynamic optimization of bioconvective non-Newtonian nanofluid systems.

2. Mathematical Model

Consider a steady two-dimensional boundary-layer flow of an incompressible, electrically conducting Eyring–Powell nanofluid containing gyrotactic microorganisms over a stretching sheet positioned along the x-axis. The flow domain is bounded within a Darcy-Forchheimer porous matrix. A uniform magnetic field of strength B_0 is applied transversely to the y-axis, giving rise to decelerating Lorentz forces. The background medium experiences internal heat generation and uniform Joule heating. Nanoparticle mass transport includes Arrhenius chemical kinetics alongside Brownian and thermophoretic slip fluxes.

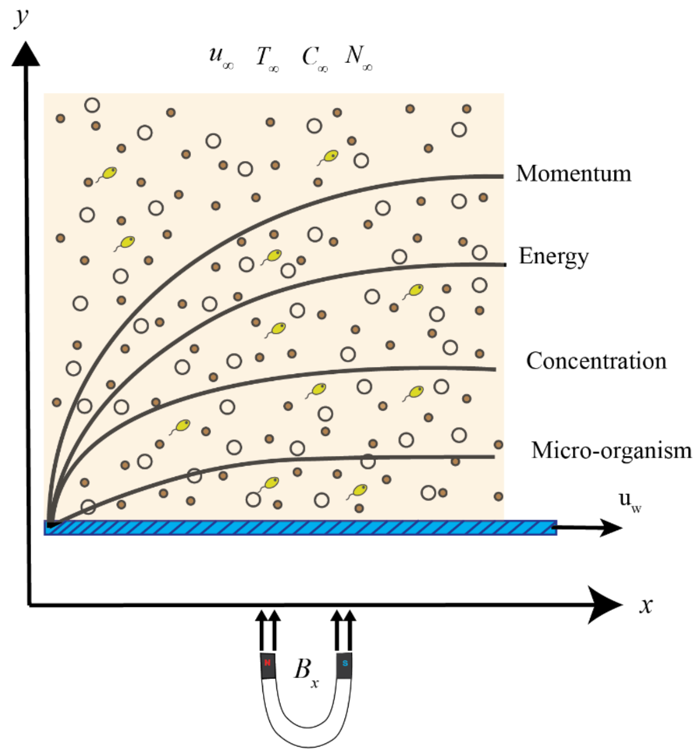

Fig.1. Physical configuration of MHD bioconvective Eyring–Powell nanofluid flow over a stretching surface situated within a Darcy–Forchheimer porous medium.

Under these boundary layer assumptions and invoking the Boussinesq approximation, the system of governing equations takes the following form [49,54]:

$$\frac{\partial u}{\partial x}+\frac{\partial v}{\partial y}=0 \quad \text{.....(1)}$$

$$u\frac{\partial u}{\partial x}+v\frac{\partial u}{\partial y}=\left(\nu+\frac{1}{\rho_f\beta_p c_p}\right)\frac{\partial^2 u}{\partial y^2}-\frac{1}{2\rho_f\beta_p c_p^3}\left(\frac{\partial u}{\partial y}\right)^2\frac{\partial^2 u}{\partial y^2}-\frac{\nu}{K_1}u-\frac{\sigma B_0^2}{\rho_f}u$$
$$+\frac{g}{\rho_f}\left[\rho_f\beta_t(T-T_\infty)+\rho_f\beta_c(C-C_\infty)-\gamma(\rho_m-\rho_f)(N-N_\infty)\right] \quad \text{.....(2)}$$

$$u\frac{\partial T}{\partial x}+v\frac{\partial T}{\partial y}=\alpha\frac{\partial^2 T}{\partial y^2}+\tau_p\left[D_B\frac{\partial C}{\partial y}\frac{\partial T}{\partial y}+\frac{D_T}{T_\infty}\left(\frac{\partial T}{\partial y}\right)^2\right]+\frac{\sigma B_0^2}{\rho_f c_f}u^2+\left(\frac{\nu}{\mathrm{c}_f}+\frac{1}{\rho_f\beta_p c_p \mathrm{c}_f}\right)\left(\frac{\partial u}{\partial y}\right)^2$$
$$+\frac{Q_0}{\rho_f c_f}(T-T_\infty)$$

…… (3)

$$u\frac{\partial C}{\partial x}+v\frac{\partial C}{\partial y}=D_B\frac{\partial^2 C}{\partial y^2}+\frac{D_T}{T_\infty}\frac{\partial^2 T}{\partial y^2}-K_r^2\left(\frac{T}{T_\infty}\right)^n\exp\left(-\frac{E_a}{\kappa T}\right)(C-C_\infty) \quad \text{……………..(4)}$$

$$u\frac{\partial N}{\partial x}+v\frac{\partial N}{\partial y}+\frac{bW_c}{C_w-C_\infty}\frac{\partial}{\partial y}\left(N\frac{\partial C}{\partial y}\right)=D_m\frac{\partial^2 N}{\partial y^2} \quad \text{…………………………...………………..(5)}$$

The relevant physical boundary conditions imposed at the solid interface and at the free stream take the form:

$$At, y=0:\ u=u_w(x)=u_0+L_1\frac{\partial u}{\partial y},\ v=0,\ -k\frac{\partial T}{\partial y}=h_f(T_f-T),\ -D_B\frac{\partial C}{\partial y}=h_c(C_f-C),$$
$$N=N_w$$

.....(6-a)

As, $y\to\infty:\ u\to 0, T\to T_\infty, C\to C_\infty, N\to N_\infty$ ………………………………..…….(6-b)

Here u and v denote velocity components in the x and y directions, respectively, while ν denotes kinematic viscosity , ρ_f represents the fluid density , β_p and c_p are Eyring-Powell material parameters , K_1 is the porous matrix permeability , F_s is the Forchheimer coefficient, σ denotes electric conductivity , B_0 represents the magnetic field intensity , g denotes the gravitational acceleration, β_t is the thermal expansion coefficient , β_c is the solutal expansion coefficient, γ is the average volume of a single microorganism, ρ_m is the microorganism mass density, α is thermal diffusivity , τ_p is the heat capacity ratio , D_B is the Brownian diffusion coefficient , D_T is the thermophoresis diffusion coefficient , c_f is the specific heat capacity , Q_0 is the volumetric heat generation coefficient, K_r^2 is the chemical reaction rate , m is the fitted non-dimensional rate constant, E_a is the Arrhenius activation energy, κ is the Boltzmann constant, D_m is the micro-organism diffusivity coefficient , b is the chemotaxis constant , W_c is the maximum cell swimming speed, $u_w(x)$ represents the stretching velocity boundary , L_1 is the velocity slip coefficient , h_f is the convective heat transfer coefficient , h_c is the convective mass transfer coefficient , T_f is hot fluid temperature , and C_f is wall-source concentration parameter constraints.

To transform the partial differential domain into a set of self-similar ordinary differential expressions, we introduce a continuous stream function $\psi(x,y)$ such that $u=\frac{\partial\psi}{\partial y}$ and $v=-\frac{\partial\psi}{\partial x}$. The similarity vector transformations are defined by:

$$\eta = y\sqrt{\frac{a}{\nu}}, \quad \psi(x,y) = \sqrt{a\nu}\,x f(\eta) \quad \theta(\eta) = \frac{T - T_\infty}{T_f - T_\infty}, \quad \phi(\eta) = \frac{C - C_\infty}{C_f - C_\infty}, \quad \chi(\eta) = \frac{N - N_\infty}{N_w - N_\infty} \quad \ldots.(7)$$

To obtain a local similarity solution, the similarity transformations are introduced into the governing equations. Since the stretching velocity varies linearly along the streamwise direction, the transformed equations are evaluated at a representative streamwise location $x = x_0$. Consequently, the streamwise coordinate is treated as a prescribed constant during the numerical computation, and all dimensionless parameters become constants. Therefore, the transformed governing equations depend only on the similarity variable η, resulting in a self-similar system of ordinary differential equations.

Substituting the similarity transformations into the governing equations and evaluating the resulting local similarity parameters at the reference streamwise location $x = x_0$ reduce the governing partial differential equations to the following nonlinear ordinary differential equations.

$$(1+\beta) f''' - \beta\epsilon(f'')(f')^2 + ff'' - (f')^2 - (M + \lambda + \frac{1}{Da})f' - Fr(f')^2 + Gr_T\theta + Gr_c\phi + Gr_m\Omega = 0 \;\ldots\ldots(8)$$

$$\frac{1}{Pr}\theta'' + f\theta' + Nb\theta'\phi' + Nt(\theta')^2 + MEc(f')^2 + Ec(1+\beta)(f'')^2 - \frac{1}{6}Ec\beta\epsilon(f'')^4 = 0 \;\ldots\ldots\ldots(9)$$

$$\phi'' + \frac{Nt}{Nb}\theta'' + Le\cdot f\phi' - Le\cdot\chi(1+\gamma_t\theta)^n \exp\left(-\frac{E}{1+\gamma_t\theta}\right)\phi = 0 \;\ldots\ldots\ldots\ldots\ldots\ldots\ldots\ldots\ldots(10)$$

$$\Omega'' + Lb\cdot f\Omega' - Pe\left[\Omega'\phi' + (\Omega + \Lambda)\phi''\right] = 0 \;\ldots\ldots\ldots\ldots\ldots\ldots\ldots\ldots\ldots\ldots\ldots\ldots(11)$$

The corresponding boundary conditions,

$$\left.\begin{array}{l} f'(0) = 1 + S_f f''(0), f(0) = 0, \Omega(0) = 1 \\ \theta'(0) = -\delta(1-\theta(0)), \phi'(0) = -\zeta(1-\phi(0)) \\ f'(\infty) \to 0, \theta(\infty) \to 0, \phi(\infty) \to 0, \Omega(\infty) \to 0 \end{array}\right\} \;\ldots\ldots\ldots\ldots\ldots\ldots\ldots\ldots\ldots\ldots\ldots\ldots\ldots(12)$$

The non-linear coupled differential boundary layer equations governing the magnetohydrodynamic bioconvective transport of Eyring-Powell nanofluids through a Darcy-Forchheimer porous medium are entirely dictated by a suite of dimensionless parameters. Here all the dimensionless parameters are defined as, fluid parameter $\beta = 1/\left(\mu\beta_p c_p\right)$, structural flow parameter $\epsilon = a^3 x_0{}^2/\left(2\nu c_p^2\right)$, magnetic parameter $M = \sigma B_0^2/\left(\rho_f a\right)$, Darcy parameter $Da = \left(K_1 a\right)/\nu$, Forchheimer inertial parameter $Fr = F_s x_0$ thermal buoyancy parameter $Gr_T = g\beta_T\left(T_f - T_\infty\right)/\left(a^2 x_0\right)$ solutal buoyancy parameter $\mathrm{Gr}_C = g\beta_c\left(C_f - C_\infty\right)/\left(a^2 x_0\right)$ bioconvection buoyancy parameter $\mathrm{Gr}_m = g\gamma\left(\rho_m - \rho_f\right)\left(N_w - N_\infty\right)/\left(\rho_f a^2 x_0\right)$ Prandtl number $Pr = \nu/\alpha$, Eckert number

$Ec = u_w^2 / \left[c_f \left(T_f - T_\infty \right) \right]$, internal heat source/sink parameter $Q = Q_0 / \left(\rho_f c_f a \right)$, Brownian motion parameter $Nb = \tau_p D_B \left(C_f - C_\infty \right) / \nu$ thermophoresis parameter $Nt = \tau_p D_T \left(T_f - T_\infty \right) / \left(\nu T_\infty \right)$ Lewis number $Le = \nu / D_B$, chemical reaction rate parameter $\chi = K_r^2 / a$, activation energy parameter $E = E_a / \left(\kappa T_\infty \right)$, the temperature ratio parameter $\gamma_t = \left(T_f - T_\infty \right) / T_\infty$, bioconvection Lewis number $Lb = \nu / D_m$, bioconvection Péclet number $Pe = bW_c / D_m$, and the microorganism concentration parameter $\Lambda = N_\infty / \left(N_w - N_\infty \right)$. Also, S_f is the velocity slip coefficient parameter, δ is the thermal Biot number, and ζ is the solutal concentration Biot number.

The skin friction coefficient (*Cf*), the Nusselt number (*Nu*), the Sherwood number (*Sh*), and motile density (*Nh*) defined as the following dimensionless form [49,54],

$$Cf = (1+\beta) f''(0) + \frac{\beta \varepsilon}{3} \left(f''(0) \right)^3, Nu = -\left(1 + \frac{4}{3} Ra \right) \theta'(0), \qquad \text{……..…………………………(13)}$$
$$Sh = -\phi'(0), Nh = -\sqrt{Re}\,\Omega'(0)$$

The resulting ordinary differential equations together with the transformed boundary conditions constitute a well-defined local similarity boundary-value problem, which is solved numerically.

3. ANALYSIS OF ENTROPY GENERATION

Evaluating the secondary irreversibility losses according to the local application of the Second Law of Thermodynamics allows us to compute local volumetric entropy rates. The dimensional entropy generation expansion rate (S''_{gen}) for an Eyring-Powell fluid under magnetohydrodynamic forces, Darcy-Forchheimer porous medium drag, Joule heating, and mass diffusion constraints is:

$$S'''_{gen} = \frac{k}{T_\infty^2} \left(\frac{\partial T}{\partial y} \right)^2 + \frac{1}{T_\infty} \left[\left(\mu + \frac{1}{\beta_p c_p} \right) \left(\frac{\partial u}{\partial y} \right)^2 - \frac{1}{6 \beta_p c_p^3} \left(\frac{\partial u}{\partial y} \right)^4 \right] + \frac{\sigma B_0^2}{T_\infty} u^2 + \frac{\mu}{K_1 T_\infty} u^2 \qquad \text{…...………(14)}$$
$$+ \frac{R D_B}{C_\infty} \left(\frac{\partial C}{\partial y} \right)^2 + \frac{R D_B}{T_\infty} \left(\frac{\partial T}{\partial y} \right) \left(\frac{\partial C}{\partial y} \right)$$

Scaling S'''_{gen} by the reference characteristic entropy generation index baseline $S_0 = \frac{k(T_f - T_\infty)^2}{T_\infty^2 L^2}$ yields the total non-dimensional localized entropy generation formulation (N_G):

$$N_G = \alpha_t (\theta')^2 + Br(1+\beta)(f'')^2 - \frac{1}{3} Br \beta \varepsilon (f'')^4 + Br(M + \frac{1}{Da})(f')^2 + \Sigma(\phi')^2 + \Sigma\zeta(\theta'\phi') \qquad \text{……(15)}$$

Where, temperature difference ratio $\alpha_t = \frac{T_f - T_\infty}{T_\infty}$, Brinkman number $Br = \frac{\mu u_w^2}{k(T_f - T_\infty)}$,concentration driven entropy parameter $\Sigma = \frac{RD_B(C_f - C_\infty)^2 \nu}{kC_\infty a x^2}$. The entropy generation number gives a quantitative measure of thermodynamic losses occurring within the system arising from heat transfer and fluid friction effects, mass diffusion, and magnetic effects. To evaluate the relative contribution of thermal irreversibility, the Bejan number (*Be*) is introduced. The Bejan number (*Be*) determines the proportion of heat transfer-induced entropy relative to total system losses:

$$Be = \frac{\alpha_t(\theta')^2}{\alpha_t(\theta')^2 + Br(1+\beta)(f'')^2 - \frac{1}{3}Br\beta\varepsilon(f'')^4 + Br(M + \frac{1}{Da})(f')^2 + \Sigma(\phi')^2 + \Sigma\zeta(\theta'\phi')} \quad \ldots\ldots(16)$$

The Bejan number varies within the interval $0 \leq Be \leq 1$. Values of $Be \to 1$ indicate dominance of heat-transfer irreversibility, whereas $Be \to 0$ correspond to irreversibility primarily caused by fluid friction, mass diffusion, and magnetic-field effects. Therefore, the Bejan number serves as an effective indicator for identifying the leading source of entropy generation within the system.

4. Numerical methodology

To obtain solutions for the boundary-value problem characterized by highly nonlinear coupled ordinary differential equations, a high-order collocation method is implemented. We transform the system into an equivalent first-order vector system by defining the state vector:

$$\vec{Y}(\eta) = [y_1, y_2, y_3, y_4, y_5, y_6, y_7, y_8]^T \quad \ldots\ldots(17)$$

$$y_1 = f, y_2 = f', y_3 = f'', y_4 = \theta, y_5 = \theta', y_6 = \varphi, y_7 = \varphi', y_8 = \Omega \quad \ldots\ldots(18)$$

The resulting differential system $\vec{Y'}(\eta) = \vec{F}(\eta, \vec{Y})$ is explicitly mapped into first-order components:

$$y_1' = y_2 \quad \ldots\ldots(19)$$

$$y_2' = y_3 \quad \ldots\ldots(20)$$

$$y_{3'} = \frac{1}{(1+\beta-\beta\epsilon y_3^2)}\left[y_2^2 - y_1 y_3 + (M + \frac{1}{Da})y_2 + Fr y_2^2 - Gr_T y_4 - Gr_C y_6 + Gr_m y_8 \right] \quad \ldots\ldots(21)$$

$$y_4' = y_5 \quad \ldots\ldots(22)$$

$$y_{5'} = -Pr\left[y_1 y_5 + Nb y_5 y_7 + Nt y_5^2 + M \cdot Ec y_2^2 + Ec(1+\beta)y_3^2 - \frac{1}{3}Ec\beta\epsilon y_3^4 + Q y_4 \right] \quad \ldots\ldots(23)$$

$$y_6' = y_7 \quad \ldots\ldots(24)$$

$$y_{7'} = -\frac{Nt}{Nb} y_{5'} - Le \cdot y_1 y_7 + Le \cdot \chi (1+\gamma_t y_4)^m \exp\left(-\frac{E}{1+\gamma_t y_4}\right) y_6 \quad \text{.................(25)}$$

$$y_{8'} = -Lb \cdot y_1 y_8 + Pe\left[y_7 y_8 + (y_8 + \Lambda) y_{7'}\right] \quad \text{..(26)}$$

The vector constraints mapped to the computational boundary conditions are:

$$\left.\begin{aligned} & y_1(0)=0, y_2(0)=1+\Omega y_3(0) \\ & y_5(0)=-\delta\left(1-y_4(0)\right),\ y_7(0)=-\zeta\left(1-y_6(0)\right),\ y_8(0)=1 \\ & y_2(\eta_\infty)=y_4(\eta_\infty)=y_6(\eta_\infty)=y_8(\eta_\infty)=0 \end{aligned}\right\} \text{.................................(27)}$$

The collocation algorithm iteratively approximates the solution over a discretized computational domain until the prescribed convergence tolerance is achieved. This approach provides accurate and stable numerical solutions for strongly coupled nonlinear systems arising in non-Newtonian nanofluid transport problems. The computational domain $[0,\eta_\infty]$ is discretized into (N) finite subintervals defined by the grid points $0=\eta_0<\eta_1<\cdots<\eta_N=\eta_\infty$. Within each subinterval $[\eta_i,\eta_{i+1}]$, the solution is approximated using a local polynomial that satisfies the governing equations at selected collocation points, which are typically chosen as Gauss–Lobatto nodes. This collocation procedure converts the differential equations into a system of nonlinear algebraic equations, expressed as, *R(U)=0.* The nonlinear system is solved iteratively using a Newton-based method. At the *k*-th iteration, the linearized system is written as

$$J\left(U^{(k)}\right)\mathit{\Delta}U = -R\left(U^{(k)}\right),$$

where (*J*) denotes the Jacobian matrix. The solution is then updated according to

$$U^{(k+1)} = U^{(k)} + \mathit{\Delta}U.$$

The iterations continue until the residual satisfies the convergence criterion $|R|_\infty < 10^{-6}$.

To improve numerical accuracy and computational efficiency, an adaptive mesh refinement procedure is employed. The mesh is automatically refined in regions where the estimated local truncation error exceeds the prescribed tolerance, thereby maintaining second- to fourth-order accuracy throughout the computational domain.

5. GRID INDEPENDENCE AND DOMAIN TRUNCATION SENSITIVITY STUDY

A grid-independence and domain-truncation study was carried out to ensure that the numerical results are both accurate and independent of the computational mesh and domain size. The purpose of this analysis was to determine an appropriate number of collocation points (*N*) and a suitable truncated boundary-layer thickness (η_∞) that could provide reliable solutions without unnecessary computational cost. The local skin-friction coefficient $-f''(0)$, local Nusselt number $-\theta'(0)$, local Sherwood number $-\phi'(0)$, and the local motile microorganism density gradient $-\Omega'(0)$ were selected as the key engineering quantities for comparison. Their values, obtained using different mesh densities and computational domains in the following **Table 1.**

Table 1: Grid-independence study for various N and η_∞ (at M = 1.0, Pr = 6.2, Da = 0.5, β = 0.7, k = 1.5, Λ = 0.07, Le = 1, Nt = 2.5, Nb = 2)

N	η_∞	$-f''(0)$	$-\theta'(0)$	$-\phi'(0)$	$-\Omega'(0)$
100	5	1.245812	0.854124	0.651241	0.9995132
150	5	1.245831	0.854195	0.651352	0.9995134
150	7	1.245831	0.854196	0.651354	0.9995135
200	5	1.245833	0.854201	0.651412	0.9995144
200	7	1.245833	0.854201	0.651412	0.9995144

The results show that increasing the number of collocation points gradually improves the numerical accuracy, while further refinement beyond N=200 produces no noticeable change in the calculated quantities. Likewise, extending the computational domain from η_∞=5 to η_∞=7 has an insignificant effect on the predicted values. In particular, for (N=200), the values of $-f''(0)$, $-\theta'(0)$, $-\phi'(0)$, and $-\Omega'(0)$ remain identical up to six decimal places for both computational domains, indicating that the numerical solution is insensitive to further domain extension. Based on these observations, a computational domain of η_∞=5 with N=200 collocation points were adopted for all subsequent simulations. This combination provides grid-independent results while satisfying the prescribed far-field boundary conditions and maintaining computational efficiency.

6. NUMERICAL VALIDATION

To verify the accuracy of the proposed numerical approach, the computed values of the local Nusselt number (Nu), Sherwood number (Sh), and skin-friction coefficient (Cf) are compared with the benchmark results of Salawu et al. [54], as summarized in Tables 1 and 2. The comparison is performed for different values of the magnetic parameter (M), microorganism concentration parameter (λ), fluid parameter (β), Darcy parameter (Da), Brownian motion parameter (Nb), Lewis number (Le), and thermophoresis parameter (Nt). The present results exhibit excellent agreement with the published data, with only negligible deviations attributable to numerical precision. This close correspondence validates the correctness of the governing equations, boundary conditions, and numerical implementation adopted in the present study, thereby confirming the reliability and robustness of the computational framework for the subsequent parametric investigations.

Table 2: Comparison of results for the Nusselt number (*Nu*) and the skin-friction coefficient (*Cf*)

M	*β*	*k*	*Λ*	*Le*	*Nt*	*Nb*	*Nu*		*Cf*	
							***Salawu et al.*[54]**	***present***	***Salawu et al.*[54]**	***present***
0.5	0.1	0.5	0.5	0.5	0.5	0.5	0.0567754	0.0566773	0.9876131	0.9876156
0.7							0.0531214	0.0531137	0.9375103	0.9375189
1.5							0.0377939	0.0378758	0.7634405	0.7634446
	0.3						0.0567917	0.0567947	1.0085264	1.0085225
	0.7						0.0568290	0.0568245	1.0613786	1.0613757
		1					0.0564705	0.0564736	0.7594454	0.7594478
		1.5					0.0562309	0.0562325	0.6100970	0.6100925
			0.03				0.0603941	0.0603957	0.9229797	0.9229713
			0.07				0.0601463	0.0601498	0.9278708	0.9278734
				0.7			0.0532639	0.0532614	0.9175590	0.9175556
				1			0.0497823	0.0497812	0.8434020	0.8434024
					1.5		0.0495253	0.0495222	1.0693535	1.0693557
					2.5		0.0407985	0.0407963	1.1842179	1.1842178
						1	0.0542505	0.0542526	1.0372375	1.0372397
						2	0.0498904	0.0498935	1.1248386	1.1248348

Table 3: Comparison of the Sherwood number (*Sh*) results

M	*β*	*k*	*Λ*	*Le*	*Nt*	*Nb*	*Sh*	
							Salawu et al.[54]	**present**
0.5	0.1	0.5	0.5	0.5	0.5	0.5	0.9371559	0.9371435
0.7							0.9433786	0.9433673
1.5							0.9704289	0.9704321
	0.3						0.9372538	0.9372163
	0.7						0.9374728	0.9374476
		1					0.9340278	0.9340341
		1.5					0.9318180	0.9318254
			0.03				0.9410089	0.9410213
			0.07				0.9401786	0.9401421
				0.7			1.1086942	1.1086231
				1			1.3208080	1.3208643
					1.5		0.9190474	0.9190320
					2.5		0.9204948	0.9204247
						1	0.9983032	0.9983213
						2	1.1709427	1.1709342

7. RESULT AND DISCUSSION

Higher permeability reduces the resistance of the porous matrix, enhancing the fluid velocity as shown in **Fig.2.** Increases in the Eyring-Powell parameter (β) reduce effective viscosity, facilitating easier flow. The synergy between low porous resistance and non-Newtonian behavior significantly broadens the momentum boundary layer.

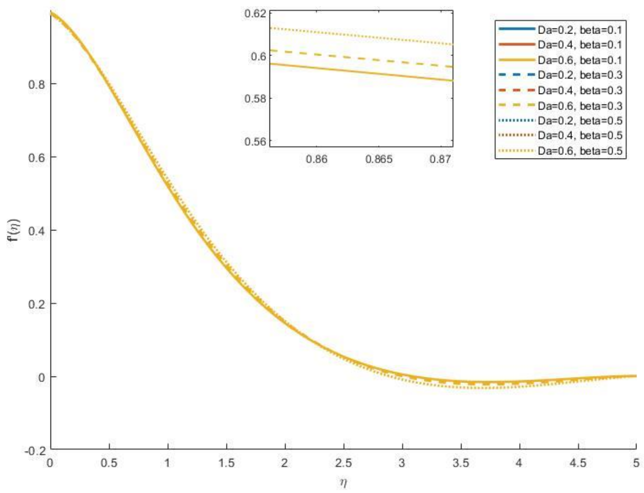

Fig.2: Impact of varying β and *Da* on *f'(η)*

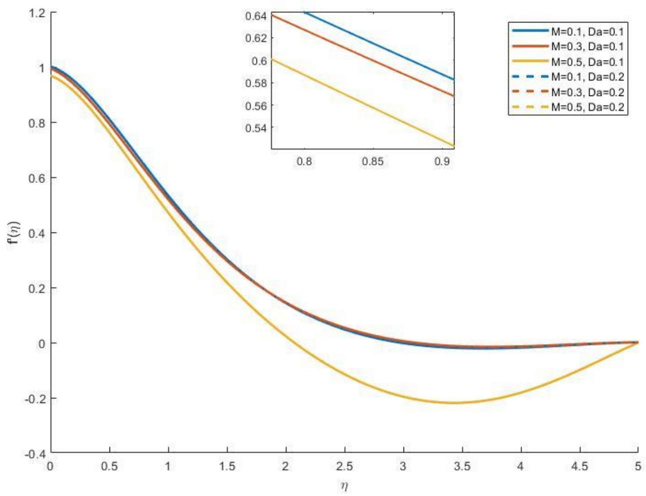

Fig.3: Competition between assistive *Da* and resistive *M* forces on *f'(η)*.

In **Fig.3**, magnetic parameter (M) generates a resistive Lorentz force acting opposite to the flow direction, thinning the boundary layer. M acts as a tuning dial for flow speed, which is critical for industrial polymer extrusion. Even under strong magnetic influence, increasing Da offsets the deceleration by providing a smoother flow path.

The thermal Grashof (Gr_T) elevates velocity profiles due to enhanced buoyancy forces near the heated stretching sheet as observed in **Fig.4**. At high Gr_T, the flow accelerates beyond the stretching rate before decaying to the ambient state. The magnetic field (M) effectively dampens this overshoot, stabilizing the boundary layer against thermal fluctuations.

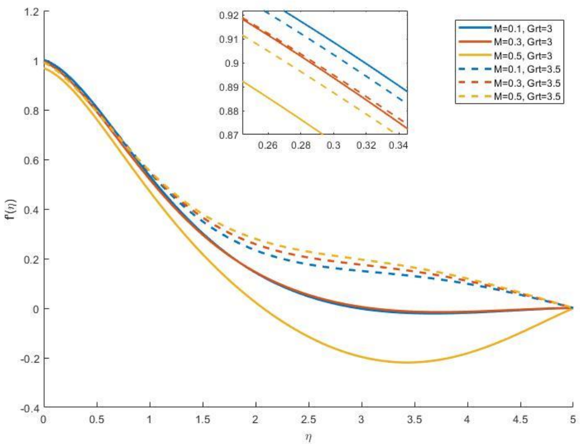

Fig.4: Impact of Gr_T on flow acceleration and magnetic damping.

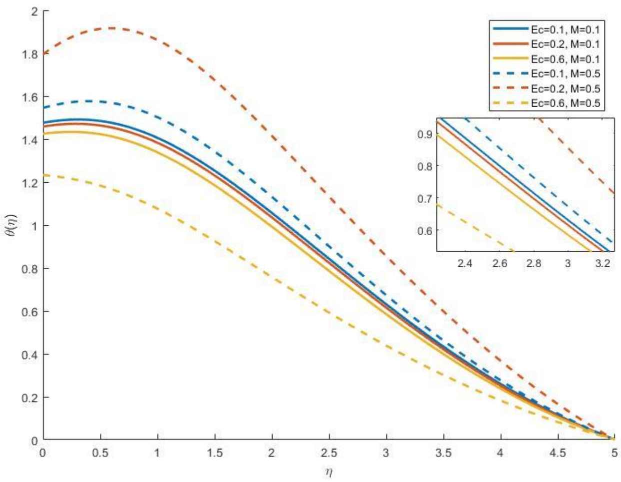

Fig.5: Temperature response to dissipative and magnetic parameters.

Higher *Ec* converts kinetic energy into thermal energy through frictional heating, raising fluid temperature. Ohmic heating (Joule effect) is amplified as the fluid works against the Lorentz force. A distinct temperature peak occurs near the wall ($\eta \approx 0.5$), indicating internal heat generation as observed in **Fig.5**.

Thermophoresis (*Nt*) facilitates the migration of particles from hot to cold regions, thickening the thermal boundary layer. Brownian motion (*Nb*) enhances thermal mixing; however, excessive *Nb* can lead to a slight reduction in peak wall temperature. As shown in **Fig.6**, *Nt* is the primary driver for thermal expansion in the nanofluid boundary layer.

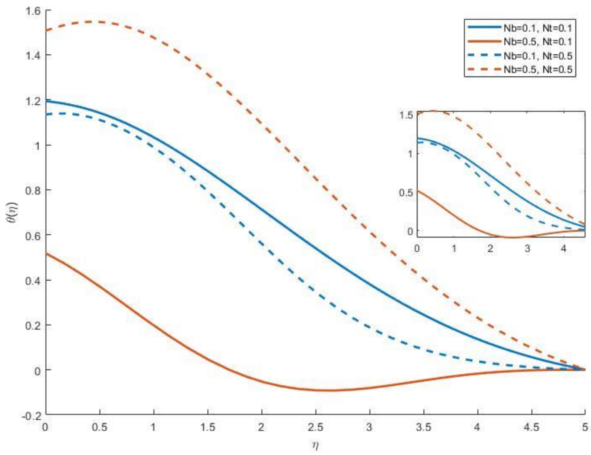

Fig. 6: Impact of thermophoresis and Brownian motion on *θ(η)*.

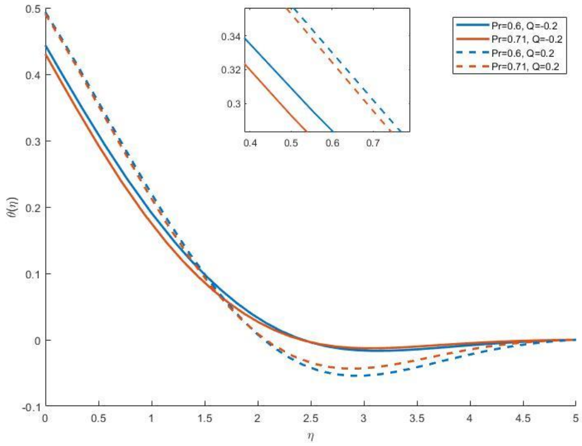

Fig.7: Cooling and heating effects under varying *Pr* and *Q*.

In **Fig.7**, a higher *Pr*, corresponding to low thermal conductivity, leads to a rapid decay in temperature profiles. A positive heat source parameter (*Q*), source, acts as an internal heater, while negative heat source parameter (*Q*), sink, provides effective cooling. Magnetic field and *Q* can be adjusted simultaneously to maintain precise thermal stability in reactors.

Increasing the fitted exponent *n* enhances the concentration of nanoparticles $\varphi(\eta)$ throughout the boundary layer shown in **Fig.8**. The interaction between reaction rates and activation energy, represented by reaction parameter χ , governs particle distribution. A higher activation energy suppresses the chemical reaction, whereas a stronger chemical reaction parameter enhances species consumption, thereby reducing the concentration boundary layer.

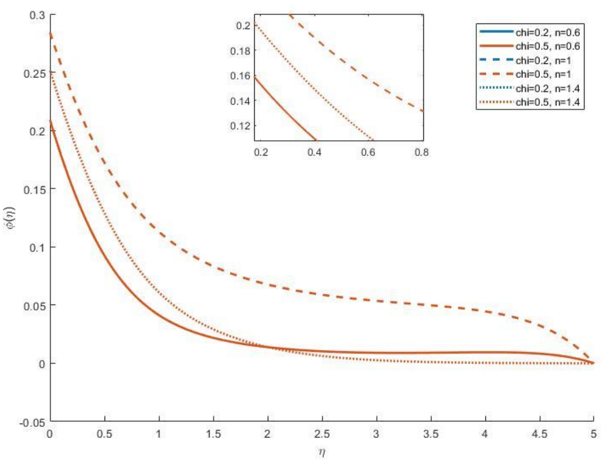

Fig. 8: Nanoparticle concentration response to reaction kinetics.

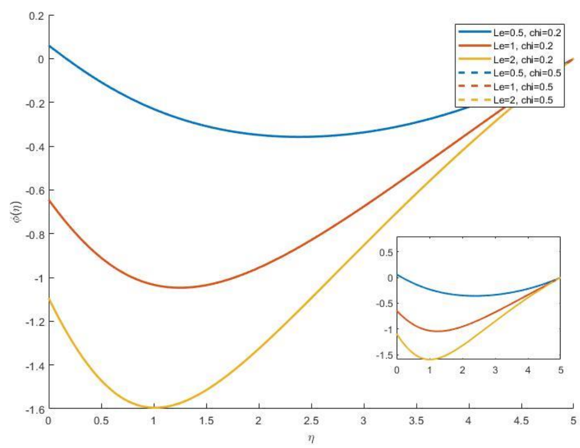

Fig.9: Influence of Lewis number on concentration boundary layer.

Higher values of *Le* result in a noticeable reduction in nanoparticle concentration profiles, as represented in **Fig. 9**. Higher *Le*, corresponding to lower mass diffusivity, restricts the penetration of nanoparticles, leading to a thinner boundary. The profiles shift downward, confirming that mass transport is inversely proportional to the thermal-to-mass diffusivity ratio.

Brownian motion (*Nb*) tends to enhance concentration as random motion assists in redistributing particles within the fluid layer. Thermophoresis (*Nt*) Exerts a resistive effect. The temperature gradient drives particles away from the heated surface toward cooler regions. While *Nt* enhances the thermal profile, it acts to reduce localized concentration, highlighting its dual physical role observed from **Fig.10**.

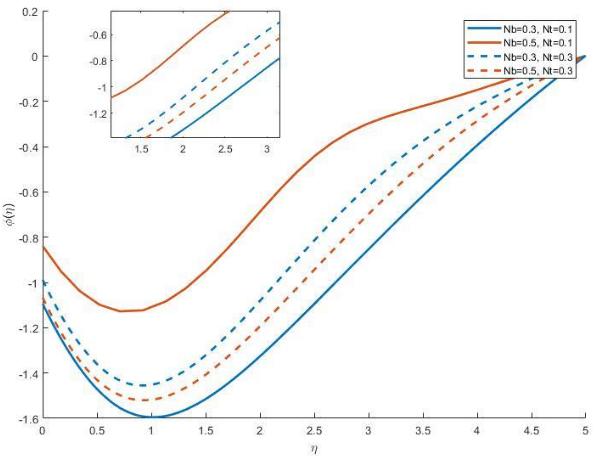

Fig.10: Competition between thermophoretic and Brownian forces.

Increasing the bioconvection Péclet number (*Pe*) reduces the microorganism density $\Omega(\eta)$. Physically, higher *Pe* implies that the directional swimming of microbes outweighs their random diffusion, narrowing the concentration layer. The bioconvection Rayleigh number (Gr_m) acts as a buoyancy force; as Gr_m increases, the microbial density profiles shift upward. From **Fig.11** it can be seen that the steepest gradients occur near the wall, where microorganisms accumulate before being dispersed by the stretching sheet motion.

In **Fig.12** higher bioconvection Lewis number (*Lb*) values correspond to a significant decrease in microbial concentration profiles. *Lb* denotes the ratio of thermal diffusivity to microorganism diffusivity. A higher value of *Lb* signifies slower microbial diffusion, restricting their spread into the ambient fluid. Managing *Pe* and *Lb* is critical for maintaining stable bioconvection plumes in bio-microfluidic devices.

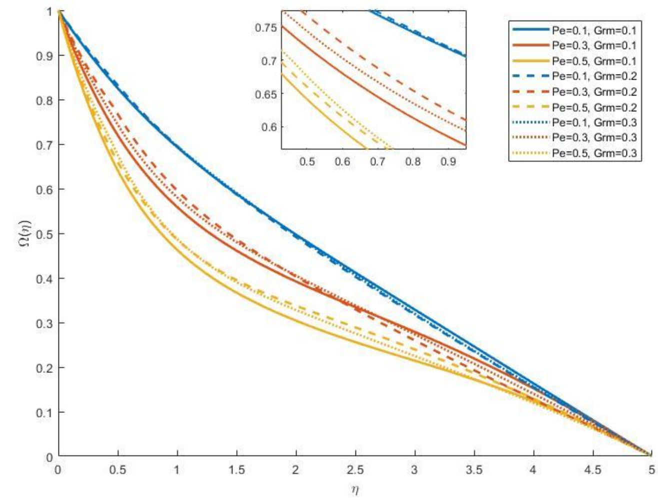

Fig.11: Microbial density response to *Pe* and Gr_m.

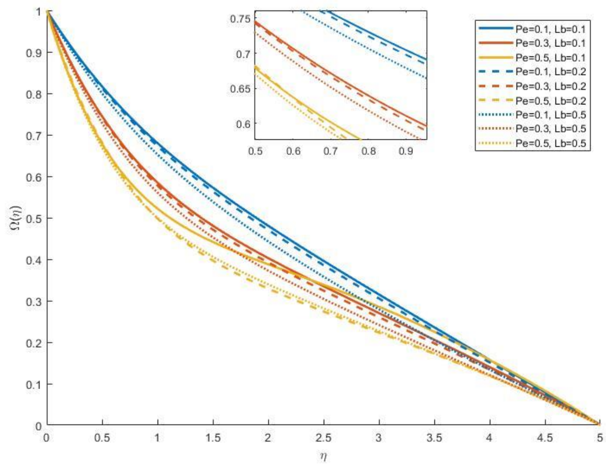

Fig.12: Variation due to the bioconvection Lewis number on $\Omega(\eta)$.

Entropy generation in the bioconvective Eyring–Powell nanofluid is controlled by three irreversibility mechanisms: heat transfer irreversibility (HTI), fluid friction irreversibility (FFI), and mass diffusion irreversibility (MDI). The results from **Fig.13** reveal that FFI is the dominant source of entropy generation under all investigated conditions, contributing significantly more than HTI and MDI. An increase in the Brinkman number (*Br*) leads to a substantial increase in fluid

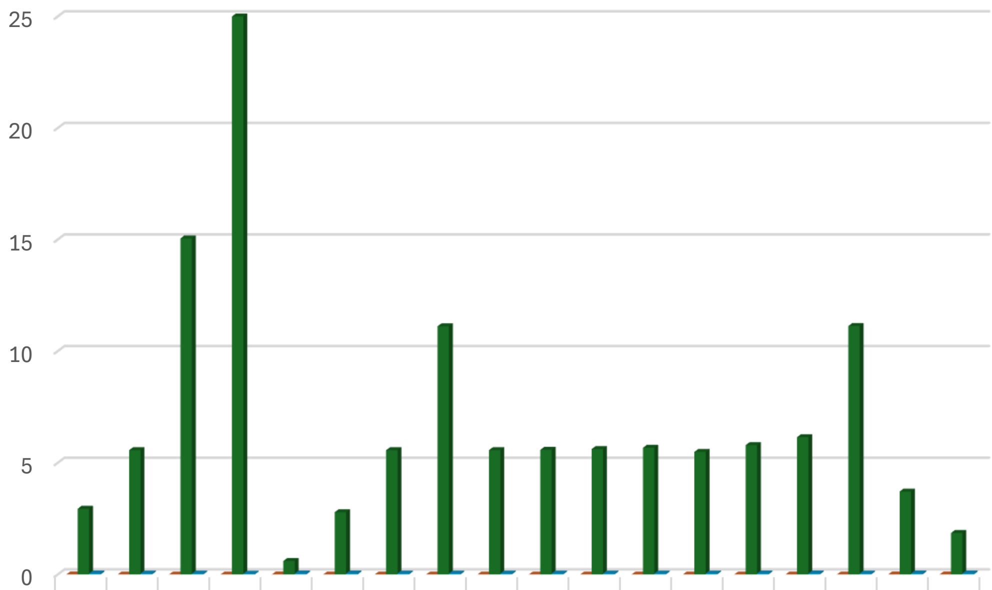

	Br	Br	Br	Br	M	M	M	M	Pe	Pe	Pe	Pe	β	β	β	ΔT	ΔT	ΔT
HTI	0	0	0	0	0	0	0	0	0	0	0	0	0	0	0	0	0	0
FFI	2.94	5.57	15.1	25	0.6	2.79	5.57	11.1	5.57	5.58	5.61	5.68	5.49	5.79	6.15	11.1	3.71	1.86
MDI	0.05	0.04	0.04	0.03	0.05	0.04	0.04	0.04	0.04	0.04	0.04	0.04	0.04	0.04	0.04	0.04	0.04	0.05

HTI FFI MDI

Fig.13: Contributions of heat transfer irreversibility (HTI), mass diffusion irreversibility (MDI), and fluid friction irreversibility (FFI) to entropy generation for varying *Br, M, Pe, β,* and *ΔT*.

friction irreversibility (FFI). This behavior occurs because a larger Brinkman number represents stronger viscous dissipation relative to conductive heat transfer, thereby increasing shear-induced energy losses and making fluid friction the dominant source of entropy generation. This indicates that viscous dissipation and velocity-gradient effects become the primary sources of energy degradation, while HTI and MDI remain comparatively small. Similarly, rising the magnetic parameter (M) enhances FFI due to the stronger Lorentz force, that suppresses fluid motion and intensifies shear-related losses. The permeability-related parameter and the non-Newtonian fluid parameter (β) also produce a moderate rise in FFI, reflecting the increased resistance to flow within the porous medium and the stronger rheological effects of the Eyring–Powell fluid. In contrast, increasing the temperature difference parameter (ΔT) shifts the entropy distribution by enhancing HTI through stronger thermal gradients while simultaneously reducing FFI as buoyancy-assisted flow weakens the near-wall shear stresses. Throughout all cases, MDI remains relatively unchanged and contributes only a minor portion of the total entropy generation, indicating that concentration-gradient effects play a secondary role in the overall irreversibility of the system.

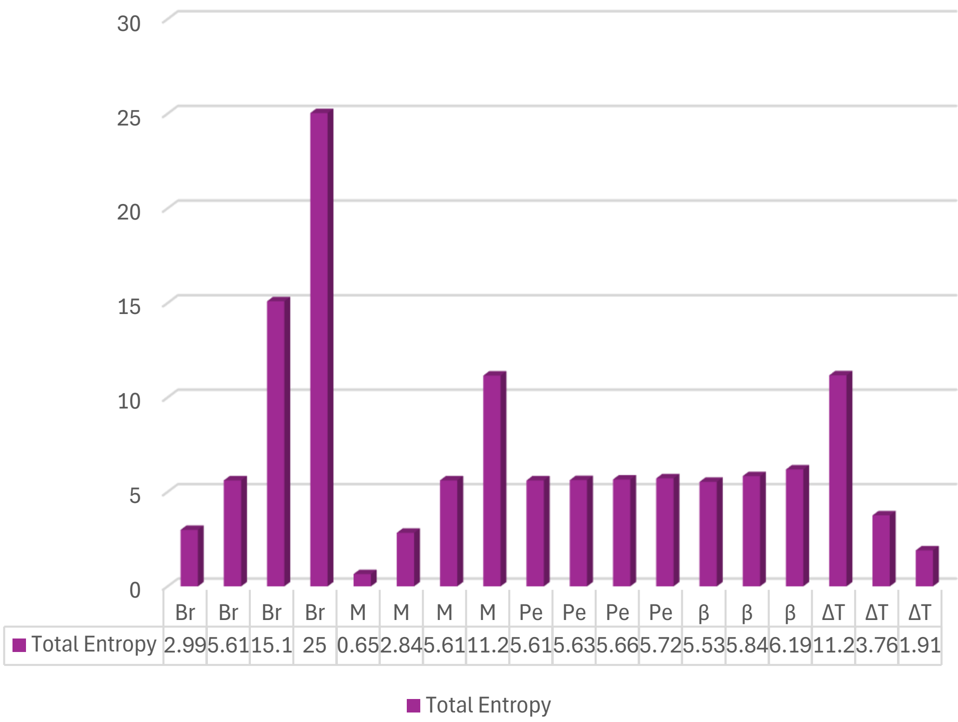

Fig.14: Effects of *Br, M, Pe, β,* and *ΔT* on the overall entropy generation rate (N_G).

The variation of the total entropy generation rate (N_G) provides an overall measure of thermodynamic irreversibility within the bioconvective Eyring–Powell nanofluid system shown in **Fig.14**. The results show that increasing the Brinkman number (*Br*) significantly increases the total entropy generation (N_G), indicating that stronger viscous dissipation enhances thermodynamic irreversibility. This behavior is consistent with Eq. (15), in which the Brinkman number directly amplifies the viscous dissipation contribution to entropy generation. A similar increasing trend is observed with the magnetic parameter (*M*), where the enhanced Lorentz force intensifies flow resistance and entropy production. In contrast, the bioconvection Péclet number (*Pe*) and fluid parameter (β) produce only moderate increases in N_G, reflecting their comparatively weaker influence on overall energy losses. Conversely, increasing the temperature difference parameter (ΔT) substantially reduces total entropy generation, suggesting that stronger thermal

buoyancy assists the flow and alleviates shear-induced irreversibilities. Overall, *Br* and *M* exert the strongest influence on entropy generation, whereas *Pe* and β have a relatively minor effect, and larger ΔT values promote a more thermodynamically efficient flow system.

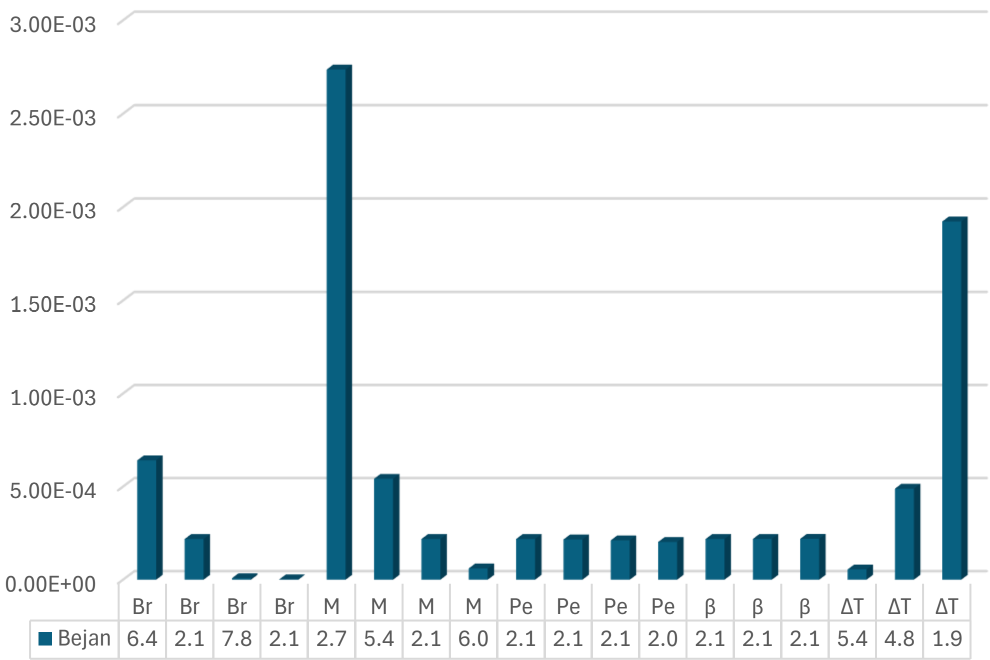

Fig.15: Response of the Bejan number (*Be*) to changes in *Br, M, Pe, β*, and *ΔT*.

The Bejan number (*Be*) is used to evaluate the contribution of heat transfer irreversibility to overall entropy generation. **Figure 15** shows that the obtained values remain very small throughout the investigated parameter range, indicating that irreversibility of the fluid friction is the dominant source of thermodynamic losses, while heat transfer irreversibility contributes only a minor portion. The results show that increasing the Brinkman number (*Br*) and magnetic parameter (*M*) reduces *Be*, as stronger viscous dissipation and Lorentz-force-induced drag enhance frictional entropy generation. The bioconvection Péclet number (*Pe*) produces only a slight decrease in *Be*, whereas the fluid parameter (β) has a negligible influence. In contrast, increasing the temperature difference parameter (*ΔT*) significantly raises the Bejan number by strengthening thermal gradients and promoting heat-transfer-related irreversibility. Overall, the analysis confirms that the entropy generation process is primarily governed by frictional effects, although thermal irreversibility becomes increasingly important at larger temperature differences.

Table 4 summarizes the respective contributions of heat transfer irreversibility (HTI), fluid friction irreversibility (FFI), and mass diffusion irreversibility (MDI) to the overall entropy generation. The results clearly show that FFI is the dominant source of entropy production under all operating conditions, while HTI and MDI contribute only marginally. Increasing (*Br*) and (*M*) significantly enhances total entropy generation, whereas larger (*ΔT*) reduces overall irreversibility and increases the Bejan number, indicating a greater contribution from heat-transfer-related entropy generation.

Table 4: Effects of *Br, M, Pe,* β, and *ΔT* on heat transfer irreversibility (HTI), fluid friction irreversibility (FFI), mass diffusion irreversibility (MDI), total entropy generation, and Bejan number.

Parameter	Value	HTI	FFI	MDI	Total Entropy	Bejan
Br	0.5	0.001916631	2.941989199	0.04537368	2.989279511	6.41×10^{-04}
Br	1	0.001225892	5.566083591	0.0444492	5.611758683	2.18×10^{-04}
Br	3	0.000118958	15.05162156	0.039602053	15.09134257	7.88×10^{-06}
Br	5	5.42×10^{-05}	24.99784734	0.0338525	25.03175401	2.17×10^{-06}
M	0.1	0.001779622	0.603369687	0.045254796	0.650404105	2.74×10^{-03}
M	0.5	0.001535958	2.789465355	0.044905871	2.835907183	5.42×10^{-04}
M	1	0.001225892	5.566083591	0.044449212	5.611758683	2.18×10^{-04}
M	2	0.000674588	11.11455814	0.043424118	11.15865684	6.05×10^{-05}
Pe	0.5	0.001225892	5.566083591	0.044449212	5.611758683	2.18×10^{-04}
Pe	1	0.001215374	5.582349678	0.044437999	5.628003051	2.16×10^{-04}
Pe	2	0.001195356	5.61435185	0.044416685	5.659963834	2.11×10^{-04}
Pe	4	0.001158698	5.67620604	0.044378106	5.721742844	2.03×10^{-04}
β	0.1	0.001208263	5.488935994	0.044405498	5.534549754	2.18×10^{-04}
β	0.5	0.001277425	5.791303723	0.04457426	5.837155408	2.19×10^{-04}
β	1	0.001359053	6.145831619	0.044764777	6.19195545	2.19×10^{-04}
Δ*T*	0.1	0.000613452	11.12764004	0.04429408	11.17254757	5.49×10^{-05}
Δ*T*	0.3	0.001837356	3.712175842	0.044598782	3.75861198	4.89×10^{-04}
Δ*T*	0.6	0.003666242	1.858114213	0.045016893	1.906797349	1.92×10^{-03}

7. CONCLUSIONS

This study numerically investigated the entropy-optimized magnetohydrodynamic bioconvective flow of an Eyring–Powell nanofluid with gyrotactic microorganisms flowing across a stretching sheet in a Darcy–Forchheimer porous medium. The formulation incorporated slip effects, Joule heating, Brownian motion, thermophoresis, and Arrhenius activation energy. The numerical results were validated against benchmark solutions and showed excellent agreement.

I. The Darcy parameter (*Da*) and fluid parameter (β) enhance fluid motion by reducing flow resistance, whereas the velocity field through the Lorentz force is suppressed by the magnetic parameter (*M*).

II. Fluid temperature rises with the Eckert number (*Ec*), Joule heating, and thermophoresis parameter (*Nt*). In contrast, larger Prandtl numbers (*Pr*) reduce thermal boundary-layer thickness and limit heat diffusion.

III. Nanoparticle concentration increases with the reaction-rate exponent and decreases with the Lewis number (*Le*). Higher bioconvection Péclet (*Pe*) and Lewis (*Lb*) numbers reduce microorganism distribution by restricting mass transport and enhancing directed swimming effects.

IV. Total entropy generation is significantly affected by the Brinkman number (*Br*) and magnetic parameter (*M*). Among all irreversibility mechanisms, fluid friction irreversibility (FFI) is the dominant contributor, while heat transfer irreversibility (HTI) and mass diffusion irreversibility (MDI) play comparatively minor roles.

V. The Bejan number remains very small throughout the investigated range, confirming the predominance of frictional losses. Increasing the temperature difference parameter (ΔT) reduces total entropy generation while increasing the proportion of heat-transfer irreversibility, leading to improved thermodynamic performance.

Overall, the findings provide useful insights for the design and optimization of advanced thermal systems involving non-Newtonian nanofluids, porous media, and bioconvective transport processes. The model may be further extended by incorporating unsteady flow effects, variable thermophysical properties, non-Fourier heat transport models, and hybrid or ternary nanofluids for future studies. The integration of machine learning and optimization techniques could also provide efficient prediction tools for entropy minimization and thermal performance enhancement in complex bio-inspired cooling and energy systems.

REFERENCES

1. Hassan AR, Gbadeyan JA, Salawu SO, The effects of thermal radiation on a reactive hydromagnetic internal heat generating fluid flow through parallel porous plates. Springer Proceedings in Mathematics and Statistics, 259:183–193, (2018). https://doi.org/10.1007/978-3-319-99719-3_17
2. Fatunmbi EO, Salawu SO, Analysis of hydromagnetic micropolar nanofluid flow past a nonlinear stretchable sheet and entropy generation with Navier slips. International Journal of Modelling and Simulation, 42:359–369, (2022). https://doi.org/10.1080/02286203.2021.1905490;WGROUP:STRING:PUBLICATION
3. Choi SUS, Enhancing thermal conductivity of fluids with nanoparticles. american society of mechanical engineers, Fluids Engineering Division (Publication) FED, 231:99–105, (1995). https://doi.org/10.1115/IMECE1995-0926
4. H. M, A. E, K. T, Alteration of thermal conductivity and viscosity of liquid by dispersing ultra-fine particles. Dispersion Of Al2o3, Sio2 and Tio2 Ultra-Fine Particles, 7:227–233, (1993). https://doi.org/10.2963/jjtp.7.227
5. Buongiorno J, Hu LW, Kim SJ, Nanofluids for enhanced economics and safety of nuclear reactors: An evaluation of the potential features issues, and research gaps. Nuclear technology, 162:80–91, (2008). https://doi.org/10.13182/NT08-A3934;PAGE:STRING:ARTICLE/CHAPTER
6. Buongiorno J, Convective transport in nanofluids. Journal of Heat Transfer, 128:240–250, (2006). https://doi.org/10.1115/1.2150834
7. Kuznetsov A V., Nield DA, Natural convective boundary-layer flow of a nanofluid past a vertical plate. International Journal of Thermal Sciences, 49:243–247, (2010). https://doi.org/10.1016/J.IJTHERMALSCI.2009.07.015

8. Roy D, Tarannum S N, Saha L K, Optimization of MHD natural convection heat and mass transfer of non-newtonian power-law ferrofluids in complex enclosures using response surface methodology. Applications in Engineering Science, 26: 100319, (2026). https://doi.org/10.1016/j.apples.2026.100319

9. Raza J, Mebarek-Oudina F, Ram P, Sharma S, MHD flow of non-newtonian molybdenum disulfide nanofluid in a converging/diverging channel with Rosseland radiation. Defect and Diffusion Forum, 401:92–106, (2020). https://doi.org/10.4028/WWW.SCIENTIFIC.NET/DDF.401.92

10. Jamshed W, Numerical investigation of MHD impact on Maxwell nanofluid. International Communications in Heat and Mass Transfer, 120:104973, (2021). https://doi.org/10.1016/J.ICHEATMASSTRANSFER.2020.104973

11. Koriko OK, Shah NA, Saleem S, Exploration of bioconvection flow of MHD thixotropic nanofluid past a vertical surface coexisting with both nanoparticles and gyrotactic microorganisms. Scientific Reports, 11:16627, (2021). https://doi.org/10.1038/s41598-021-96185-y

12. Li YX, Alshbool MH, Lv YP, Heat and mass transfer in MHD Williamson nanofluid flow over an exponentially porous stretching surface. Case Studies in Thermal Engineering, 26:100975, (2021). https://doi.org/10.1016/J.CSITE.2021.100975

13. Abbas SZ, Khan MI, Kadry S, Fully developed entropy optimized second order velocity slip MHD nanofluid flow with activation energy. Computer Methods and Programs in Biomedicine, 190:105362, (2020). https://doi.org/10.1016/J.CMPB.2020.105362

14. Dawar A, Shah Z, Kumam P, Chemically reactive MHD micropolar nanofluid flow with velocity slips and variable heat source/sink. Scientific Reports, 10:20926, (2020). https://doi.org/10.1038/s41598-020-77615-9

15. Shi QH, Hamid A, Khan MI, Numerical study of bio-convection flow of magneto-cross nanofluid containing gyrotactic microorganisms with activation energy. Scientific Reports, 11:16030, (2021). https://doi.org/10.1038/s41598-021-95587-2

16. Ashraf MZ, Rehman SU, Farid S, Insight into significance of bioconvection on MHD tangent hyperbolic nanofluid flow of irregular thickness across a slender elastic surface. Mathematics, Vol 10, Page 2592 10:2592, (2022). https://doi.org/10.3390/MATH10152592

17. Ali L, Ali B, Liu X, A comparative study of unsteady MHD Falkner–Skan wedge flow for non-Newtonian nanofluids considering thermal radiation and activation energy. Chinese Journal of Physics, 77:1625–1638, (2022). https://doi.org/10.1016/J.CJPH.2021.10.045

18. Habib D, Salamat N, Abdal SHS, Ali B, Numerical investigation for MHD Prandtl nanofluid transportation due to a moving wedge: Keller box approach. International Communications in Heat and Mass Transfer, 135:106141, (2022). https://doi.org/10.1016/J.ICHEATMASSTRANSFER.2022.106141

19. Ree T, Eyring H, Theory of Non-Newtonian Flow. I. Solid Plastic System. Journal of Applied Physics, 26:793–800, (1955). https://doi.org/10.1063/1.1722098

20. Wang J, Mustafa Z, Siddique I, Computational analysis for bioconvection of microorganisms in prandtl nanofluid darcy–forchheimer flow across an inclined sheet. Nanomaterials, Vol 12, Page 1791 12:1791, (2022). https://doi.org/10.3390/NANO12111791

21. Younis O, Alizadeh M, Kadhim H, MHD natural convection and radiation over a flame in a partially heated semicircular cavity filled with a nanofluid. Mathematics, Vol 10, Page 1347 10:1347, (2022). https://doi.org/10.3390/MATH10081347

22. Ali L, Ali B, Liu X, Analysis of bio-convective MHD Blasius and Sakiadis flow with Cattaneo-Christov heat flux model and chemical reaction. Chinese Journal of Physics, 77:1963–1975, (2022). https://doi.org/10.1016/J.CJPH.2021.12.008

23. Gupta RK, Sridhar T, Viscoelastic effects in non-Newtonian flows through porous media. Rheologica Acta, 24:148–151, (1985). https://doi.org/10.1007/BF01333242/METRICS

24. Prasad K V., Abel MS, Khan SK, Momentum and heat transfer in visco-elastic fluid flow in a porous medium over a non-isothermal stretching sheet. The International Journal of Numerical Methods for Heat & Fluid Flow, 10:786–801, (2000). https://doi.org/10.1108/09615530010359102
25. Seddeek MA, Salama FA, The effects of temperature dependent viscosity and thermal conductivity on unsteady MHD convective heat transfer past a semi-infinite vertical porous moving plate with variable suction. Computational Materials Science, 40:186–192, (2007). https://doi.org/10.1016/J.COMMATSCI.2006.11.012
26. Zheng L, Zhang C, Zhang X, Zhang J, Flow and radiation heat transfer of a nanofluid over a stretching sheet with velocity slip and temperature jump in porous medium. Journal of the Franklin Institute, 350:990–1007, (2013). https://doi.org/10.1016/J.JFRANKLIN.2013.01.022
27. Vishalakshi AB, Mahabaleshwar US, Sheikhnejad Y, Impact of MHD and mass transpiration on rivlin–ericksen liquid flow over a stretching sheet in a porous media with thermal communication. Transport in Porous Media, 2022 142:1 142:353–381, (2022). https://doi.org/10.1007/S11242-022-01756-W
28. Kothandapani M, Srinivas S, Peristaltic transport of a Jeffrey fluid under the effect of magnetic field in an asymmetric channel. International Journal of Non-Linear Mechanics, 43:915–924, (2008). https://doi.org/10.1016/J.IJNONLINMEC.2008.06.009
29. Mahabaleshwar US, Anusha T, Hatami M, The MHD Newtonian hybrid nanofluid flow and mass transfer analysis due to super-linear stretching sheet embedded in porous medium. Scientific Reports, 2021 11:1 11:22518, (2021). https://doi.org/10.1038/s41598-021-01902-2
30. Dessie H, Kishan N, MHD effects on heat transfer over stretching sheet embedded in porous medium with variable viscosity, viscous dissipation and heat source/sink. Ain Shams Engineering Journal, 5:967–977, (2014). https://doi.org/10.1016/J.ASEJ.2014.03.008
31. Nadeem S, Akbar NS, Influence of heat transfer on a peristaltic flow of Johnson Segalman fluid in a non-uniform tube. International Communications in Heat and Mass Transfer, 36:1050–1059, (2009). https://doi.org/10.1016/J.ICHEATMASSTRANSFER.2009.07.012
32. Mekheimer KS, Abd elmaboud Y, Peristaltic flow of a couple stress fluid in an annulus: Application of an endoscope. Physica A: Statistical Mechanics and its Applications, 387:2403–2415, (2008). https://doi.org/10.1016/J.PHYSA.2007.12.017
33. Hayat T, Momoniat E, Mahomed FM, Peristaltic MHD flow of third grade fluid with an endoscope and variable viscosity. Journal of Nonlinear Mathematical Physics, 15:91–104, (2008).
34. Mekheimer KS, Effect of the induced magnetic field on peristaltic flow of a couple stress fluid. Physics Letters A, 372:4271–4278, (2008). https://doi.org/10.1016/J.PHYSLETA.2008.03.059
35. Srinivas S, Gayathri R, Kothandapani M, The influence of slip conditions, wall properties and heat transfer on MHD peristaltic transport. Computer Physics Communications, 180:2115–2122, (2009). https://doi.org/10.1016/J.CPC.2009.06.015
36. Bilal M, Ashbar S, Flow and heat transfer analysis of Eyring-Powell fluid over stratified sheet with mixed convection. Journal of the Egyptian Mathematical Society Bilal and Ashbar Journal of the Egyptian Mathematical Society, 28:40, (2020). https://doi.org/10.1186/s42787-020-00103-6
37. Sher Akbar N, Ebaid A, Khan ZH, Numerical analysis of magnetic field effects on Eyring-Powell fluid flow towards a stretching sheet. Journal of Magnetism and Magnetic Materials, 382:355–358, (2015). https://doi.org/10.1016/J.JMMM.2015.01.088
38. Ibrahim W, Hindebu B, Magnetohydrodynamic (MHD) boundary layer flow of Eyring-Powell nanofluid past stretching cylinder with Cattaneo-Christov heat flux model. Nonlinear Engineering, 8:303–317, (2019). https://doi.org/10.1515/NLENG-2017-0167/XML
39. Javed T, Ali N, Abbas Z, Sajid M, Flow of an eyring-powell non-newtonian fluid over a stretching sheet. Chemical Engineering Communications, 200:327–336, (2013). https://doi.org/10.1080/00986445.2012.703151

40. Sreenivasulu P, Poornima T, Malleswari B, Internal energy activation stimulus on magneto-bioconvective Powell-Eyring nanofluid containing gyrotactic microorganisms under active/passive nanoparticles flux. Physica Scripta, 96:055221, (2021). https://doi.org/10.1088/1402-4896/ABEB33

41. Mustafa M, Khan JA, Hayat T, Alsaedi A, Buoyancy effects on the MHD nanofluid flow past a vertical surface with chemical reaction and activation energy. International Journal of Heat and Mass Transfer, 108:1340–1346, (2017). https://doi.org/10.1016/J.IJHEATMASSTRANSFER.2017.01.029

42. Ijaz M, Ayub M, Khan H, Entropy generation and activation energy mechanism in nonlinear radiative flow of Sisko nanofluid: rotating disk. Heliyon, 5:e01863, (2019). https://doi.org/10.1016/j.heliyon.2019.e01863

43. Salawu SO, Hassan AR, Abolarinwa A, Oladejo NK, Thermal stability and entropy generation of unsteady reactive hydromagnetic Powell-Eyring fluid with variable electrical and thermal conductivities. Alexandria Engineering Journal, 58:519–529, (2019). https://doi.org/10.1016/J.AEJ.2019.05.004

44. Rashidi MM, Ali M, Freidoonimehr N, Nazari F, Parametric analysis and optimization of entropy generation in unsteady MHD flow over a stretching rotating disk using artificial neural network and particle swarm optimization algorithm. Energy, 55:497–510, (2013). https://doi.org/10.1016/J.ENERGY.2013.01.036

45. Waleed Ahmed Khan M, Ijaz Khan M, Hayat T, Alsaedi A, Entropy generation minimization (EGM) of nanofluid flow by a thin moving needle with nonlinear thermal radiation. Physica B: Condensed Matter, 534:113–119, (2018). https://doi.org/10.1016/J.PHYSB.2018.01.023

46. Salawu SO, Oke SI, Inherent Irreversibility of Exothermic Chemical Reactive Third-Grade Poiseuille Flow of a Variable Viscosity with Convective Cooling. Journal of Applied and Computational Mechanics, 4:167–174, (2018). https://doi.org/10.22055/JACM.2017.22933.1144

47. Hayat T, Khan SA, Ijaz Khan M, Alsaedi A, Theoretical investigation of Ree-Eyring nanofluid flow with entropy optimization and Arrhenius activation energy between two rotating disks. Computer Methods and Programs in Biomedicine, 177:57–68, (2019). https://doi.org/10.1016/J.CMPB.2019.05.012

48. Khan NM, Dynamics of motile gyrotactic microorganisms in a steady Eyring-Powell nanofluid flow with nonlinear thermal radiation and suction, (2022) https://doi.org/10.21203/rs.3.rs-1447649/v1

49. Reddy, M. V., Ajithkumar, M., Ali, F., Reddy, K. V., & Khan, U., Entropy optimization in magneto nonlinear mixed convective flow of Ree-Eyring nanofluid with activation energy and gyrotactic microorganisms. Journal of Nonlinear Mathematical Physics, 32(1), 47, (2025). https://doi.org/10.1007/s44198-025-00300-w

50. Salawu SO, Hassan AR, Abolarinwa A, Oladejo NK, Thermal stability and entropy generation of unsteady reactive hydromagnetic Powell-Eyring fluid with variable electrical and thermal conductivities. Alexandria Engineering Journal, 58:519–529, (2019). https://doi.org/10.1016/J.AEJ.2019.05.004

51. Salawu SO, Oke SI, Inherent Irreversibility of Exothermic Chemical Reactive Third-Grade Poiseuille Flow of a Variable Viscosity with Convective Cooling. Journal of Applied and Computational Mechanics, 4:167–174, (2018). https://doi.org/10.22055/JACM.2017.22933.1144

52. Rashidi MM, Mohammadi F, Abbasbandy S, Alhuthali MS, Available online at www.jafmonline.net. Journal of Applied Fluid Mechanics, 8:1735–3645, (2015). https://doi.org/10.18869/acadpub.jafm.67.223.22916

53. Waleed Ahmed Khan M, Ijaz Khan M, Hayat T, Alsaedi A, Entropy generation minimization (EGM) of nanofluid flow by a thin moving needle with nonlinear thermal radiation. Physica B: Condensed Matter, 534:113–119, (2018). https://doi.org/10.1016/J.PHYSB.2018.01.023

54. Salawu SO, Kareem RA, Ajilore JO, Eyring-Powell MHD nanoliquid and entropy generation in a porous device with thermal radiation and convective cooling. Journal of the Nigerian Society of Physical Sciences, 4:924–924, (2022). https://doi.org/10.46481/jnsps.2022.924